Journal of Neuroscience Methods 295 (2018) 37–44

Contents lists available at ScienceDirect

Journal of Neuroscience Methods

journal homepage: www.elsevier.com/locate/jneumeth

Three-dimensional imaging and analysis of entire peripheral nerves after repair and reconstruction

Christos Bikis[a], Lucas Degrugillier[b], Peter Thalmann[a], Georg Schulz[a], Bert Müller[a,***], Simone E. Hieber[a,*], Daniel F. Kalbermatten[c,d], Srinivas Madduri[b,c,e,**]

[a] Biomaterials Science Center, Department of Biomedical Engineering, University of Basel, Switzerland
[b] Center for Bioengineering and Regenerative Medicine, Department of Biomedical Engineering, University of Basel, Switzerland
[c] Department of Plastic, Reconstructive, Aesthetic and Hand Surgery, Basel University Hospital, Switzerland
[d] Department of Pathology, Basel University Hospital, Switzerland
[e] Department of Biomedicine, University of Basel, Switzerland

HIGHLIGHTS

- Micro-scale details of 3D nerve fiber and vessel reorganization upon repair.
- Distinct differentiation between nerve and connective tissue in a label-free manner.
- Perineurium membranes and small capillaries visualized with isotropic 4 μm resolution.
- Quantitative measures proved significance for assessing repair quality, $p < 0.01$.

GRAPHICAL ABSTRACT

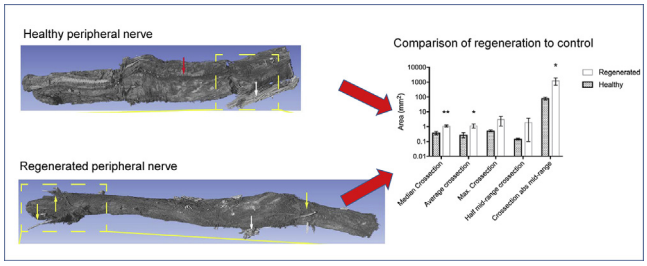

ARTICLE INFO

Article history:
Received 26 August 2017
Received in revised form
23 November 2017
Accepted 23 November 2017
Available online 26 November 2017

Keywords:
μCT
X-ray tomography
Axonal regeneration
Anatomy
Morphology
Micrometer
Non-destructive
Nerve conduits
Nerve reconstruction
3D imaging

ABSTRACT

Background: We wanted to achieve a three-dimensional (3D), non-destructive imaging and automatic post-analysis and evaluation of reconstructed peripheral nerves without involving cutting and staining processes.
New method: We used a laboratory-based micro computed tomography system for imaging, as well as a custom analysis protocol. The sample preparation was also adapted in order to achieve 3D images with true micrometer resolution and suitable contrast.
Results: Analysis of the acquired tomograms enabled the quantitative assessment of 3D tissue structures, i.e., surface morphology, nerve fascicles, nerve tissue volume, geometry, and vascular regrowth. The resulting data showed significant differences between operated animals and non-operated controls.
Comparison with existing methods: Our approach avoids the sampling error associated with conventional 2D visualization approaches and holds promise for automation of the analysis of large series of datasets.
Conclusions: We have presented a potential way for 3D imaging and analysis of entire regenerated nerves non-destructively, paving the way for high-throughput analysis of therapeutic conditions of treating adult nerve injuries.

Abbreviations: NC, nerve conduit; μCT, X-ray microtomography; ROI, region of interest; SNR, signal-to-noise-ratio.

* Corresponding author at: Biomaterials Science Center, Department of Biomedical Engineering, University of Basel, Gewerbestrasse 14, 4123 Allschwil, Switzerland.
** Corresponding author at: Center for Bioengineering and Regenerative Medicine, Department of Biomedical Engineering, University Hospital Basel, Spitalstrasse 21/Petersgraben 4, 4031 Basel, Switzerland.
*** Corresponding author at: Biomaterials Science Center, Department of Biomedical Engineering, University of Basel, Gewerbestrasse 14, 4123 Allschwil, Switzerland.
E-mail addresses: bert.mueller@unibas.ch (B. Müller), simone.hieber@unibas.ch (S.E. Hieber), srinivas.madduri@unibas.ch (S. Madduri).

https://doi.org/10.1016/j.jneumeth.2017.11.015

1. Introduction

Peripheral nerve injuries constitute a medical problem of considerable significance, both in the clinic, as well as in research. Reported cases show an increasing prevalence, with several hundred thousand new patients affected annually (Kingham and Terenghi, 2006). Furthermore, the capacity of the nervous system for self-healing is a priori limited compared to other systems (Hsu et al., 2013). Taken together, these two factors contribute to a substantial socio-economical burden, associated with work leave, health care expenses and chronic disability.

As far as the existing therapeutic interventions are concerned, end-to-end suturing and autologous nerve grafting are the current choices of treatment (Haftek, 1976; Stang et al., 2005). Nevertheless, axonal regeneration very often remains challenging and the functional outcome is unsatisfactory. In detail, end-to-end suturing leads to a reduced stretching capacity in almost one out of four cases, due to morphological and micro-anatomical alterations at the site of the intervention. These drawbacks include the effects of Wallerian degeneration, as well as fibrosis and tissue adhesions occurring both around and inside the nerve (Kannan et al., 2005). When the direct end-to-end suturing is not an option, nerve grafting is needed, autologous grafts being the gold standard. Nevertheless, this approach is still associated with several shortcomings such as scar formation, donor site morbidity, size and modality mismatch (Johnson et al., 2005; Weis et al., 2012).

It is for all the above reasons that research on biodegradable nerve conduits (NC) has gained increasing importance over the last 30 years (Madduri and Gander, 2012). A variety of materials are used with or without growth promoting agents, allowing for the nerve to regrow inside the NC. However, full functional recovery itself remains an unmet challenge (Yang et al., 2007; Moore et al., 2009). Furthermore, the returning of function depends to some extent on the exact 3D microanatomy of the nerve, as well as the morphology of the conduit-nerve complex. However, histology, which is the gold standard of assessing anatomical recovery, is inherently 2D. Therefore, it should ideally be complemented by a compatible, 3D approach. Currently, ultrasonography (US) and magnetic resonance imaging (MRI) are being used in clinical practice for the 3D imaging of peripheral nerves, in particular for diagnosis and for monitoring peripheral neuropathies (Garg et al., 2017; Wu et al., 2017; Walker, 2017; Willsey et al., 2017). The spatial resolution, however, is limited to a fraction of a millimeter (Willsey et al., 2017). The 3D imaging of peripheral nerves by US and MRI with true micrometer resolution, however, remains elusive.

Towards this goal, recent developments include the visualization of rat sciatic nerves by a laboratory micro computed tomography (μCT) system, using Lugol's iodine (Hopkins et al., 2015; Pixley et al., 2016). Aiming to eliminate the need for a contrast agent, we have illustrated the use of a laboratory μCT system for the visualization and quantification of unstained, paraffin-embedded reconstructed nerves inside a collagen NC (Bikis et al., 2016, 2017). The visualization is perfectly compatible with histological studies based on paraffin embedding. In particular, the non-destructive micro computed tomography measurements can be carried out directly after paraffin embedding and prior to the histological evaluation, with the only added process step of melting the cylindrically shaped paraffin-embedded tissue to obtain the standard histological paraffin block for the subsequent histological sectioning.

In this study, we have improved both the spatial resolution and contrast, achieving high-resolution 3D imaging of regenerated nerves by using advanced laboratory-based μCT, where the spatial resolution was better than the distance between neighboring slices for typical histological sectioning. For this, we prepared collagen NC and implanted them in rats to bridge a 10 mm-long sciatic nerve gap injury. Three months post-operatively, regenerated nerve tissue was explanted and processed for imaging. The increase in spatial resolution was coupled with an increase in the contrast difference between anatomical structures, owing to an improved scanning and data treatment procedure. Thus, the enhanced image quality appears to be sufficient to assess the regenerated peripheral nerves in a truly 3D way, down to the true micrometer level. Hopkins et al. (2015) have already demonstrated a clear relation between the anatomical features of examined nerves recognized in micro computed tomography and histology. As consequence, the authors have focused the study on the three-dimensional CT images. For the investigated nerves, surface landmarks of the sample can also be identified, allowing for the selection of the optimal cutting plane for the histological slices (Stalder et al., 2014). This study paves the way for the standardization of the non-destructive monitoring of regenerated nerves and eventually for high throughput analysis in the field of nerve regeneration.

2. Materials and methods

2.1. NC fabrication

Collagen NCs were produced using spinning mandrel technology, as illustrated previously (Madduri et al., 2010). Insoluble collagen (2.5%, w/w) was swollen in 1 M acetic acid and then homogenized with a high-speed mixer at 10,000 rpm (Polytron®, Kinematica, Lucerne, Switzerland) for a duration of 1 min. The homogeneous collagen dispersion was applied via a syringe onto a spinning gold-coated mandrel (diameter of 1.5 mm), installed in a sideways reciprocating apparatus, and the solvent was dried off under laminar airflow. Subsequently, the resulting tubes were neutralized by incubation in 0.1 M di-sodium hydrogen phosphate (pH of 7.4) for 1 h. The tubes were finally cut into 14 mm long specimens, which were cross-linked by subjecting the collagen tubes to a dehydro-thermal treatment (DHT) at a temperature of 110 °C and a pressure of 20 mbar for a period of 5 days. The resulting tubes exhibited an outer and inner diameter of 2.5 mm and 1.5 mm, respectively.

2.2. Animal experiments

All animals were treated in compliance with the ethical permission approved (25,212) from the Veterinary Office of the Kanton Basel-Stadt (Basel, Switzerland). Three female Sprague Dawley rats weighing 250–300 g, about eight weeks old, were housed under standard temperature and light conditions. Left sciatic nerve was surgically operated for creating 10 mm gap. The resulting nerve gap was bridged using 14 mm collagen NC (Madduri et al., 2010) and explanted 12 weeks post-operatively for outcome analysis. The normal nerves were collected from the un-operated side of the same animals, thus respecting the 3Rs of the animal experimentation.

2.3. Standard histological processing

After excision, the peripheral nerves were processed following a standard histology protocol for formalin fixation–paraffin embedding. In detail, after excision, the nerves were straightened by firmly tugging them from both ends by means of surgical forceps, fixed in histology-grade formalin, and dehydrated in ascending ethanol solutions. Subsequently, they were transferred to xylol and then perfused in a liquid paraffin–polymer mixture (Leica Paraplast). The long healthy nerve was cut in two parts and resulting segments were placed longitudinally away from each other, thus creating the gap between the two nerve segments that may represent the artificial nerve gap created in the present study. Unless otherwise stated,

such gap was only for experimental characterization and excluded from the further measurement analysis.

2.4. Paraffin sample processing specific for X-ray imaging

When liquid paraffin perfusion was completed, the nerves were removed from the histological tissue processor, placed in a metal container and left for 24 h inside an oven at a temperature of 60 °C. This step is important in removing the majority of air bubbles trapped inside or around the specimen, that can cause artifacts during the X-ray imaging and make data analysis more complex. Afterwards, the specimens were thoroughly washed under flowing liquid paraffin, to remove high-absorbing particles or debris on the sample surface that would affect imaging quality. Finally, the nerve was dipped in paraffin several times while holding from one edge, until a uniform cylinder-like specimen was formed and then cooled down to 4 °C during a period of 15 min.

2.5. Mounting of samples on holders compatible with the laboratory μCT system

In the end, the paraffin samples were glued to specialized metal sample holders using a cyanoacrylate glue. Care was taken to ensure that the glue would cover a small area of the nerve bottom. Handling of the specimen was performed exclusively by forceps to avoid deposits on the sample surface that would cause imaging artifacts. After the glue settled, any excess was removed carefully by a scalpel and the specimens were ready for the X-ray imaging.

2.6. Tomography measurements and reconstruction

For the X-ray tomography measurements, we used the μCT laboratory system phoenix nanotom® m (phoenix |X-ray, GE Sensing & Inspection Technologies GmbH, Wunstorf, Germany). An acceleration voltage of 60 kV and a beam current of 280 mA were selected for the operation of the X-ray beam. Over an angular range of 360 °, 1800 projections were acquired. The effective pixel size was 4 μm and scanning time was 2.5 h for a 1 cm-long nerve. After reconstruction, the 16-bit dataset is approximately 2 GB in size.

2.7. Data handling and visualization

For the orientation within the large datasets acquired, a commercially available software is needed. The VGStudio MAX 2.1 (Volume Graphics GmbH, Heidelberg, Germany) was thus used both for the three-dimensional rendering and the visualization of the acquired tomograms, cp. images in Figs. 1 and 5.

2.8. Data analysis

The entire process of the automated analysis is explained in detail in Bikis et al. (2017). Shortly, the nerves were segmented from their surroundings by means of an intensity thresholding/median filtering/connected component analysis. After nerve segmentation, extraction of the investigated parameters was performed in a fully automated way. For these tasks, Matlab (MATLAB 2016a, The MathWorks, Inc., Natick, Massachusetts, United States) was used. The diagrams in Fig. 3 where prepared using the pro Fit software (pro Fit 6.2.16, Quantum Soft, Uetikon am See, Switzerland). For the statistical analysis, the data were expressed as means ± SE. Student's t test was used to determine statistical significance of differences ($p < 0.05$ was considered statistically significant). The statistical analysis was performed in GraphPad Prism 7.00 for Mac (GraphPad Software, La Jolla California USA).

3. Results

3.1. Surface morphology

An inherent advantage of tomography with respect to traditional 2D imaging approaches is the isotropic voxel resolution provided, enabling accurate surface reconstruction, by means of 3D rendering, which is exemplarily demonstrated in the present study. In Fig. 1, a healthy and a regenerated nerve are rendered, with their proximal and distal ends located at 2 mm from the right and left borders of the images, respectively.

For the reconstructed nerve, starting near its proximal end, the marking sutures and the scarring that has occurred around them are visible (yellow-colored arrow). Muscle fibers attached to the nerve surface (white-colored arrow) are also visible close to the proximal nerve end. The middle section of the reconstructed nerve shows a reduced diameter with respect to the ends. A line plot of the cross sectional area is presented below. The distal nerve end is presented in larger magnification in Fig. 1(b, bottom), which shows how the fibrinoid tissue envelops the sutures.

For the overview image of the healthy nerve (Fig. 1a, top), presented for comparison, the most prominent difference to the reconstructed nerve is the major surface groove (red arrow) caused

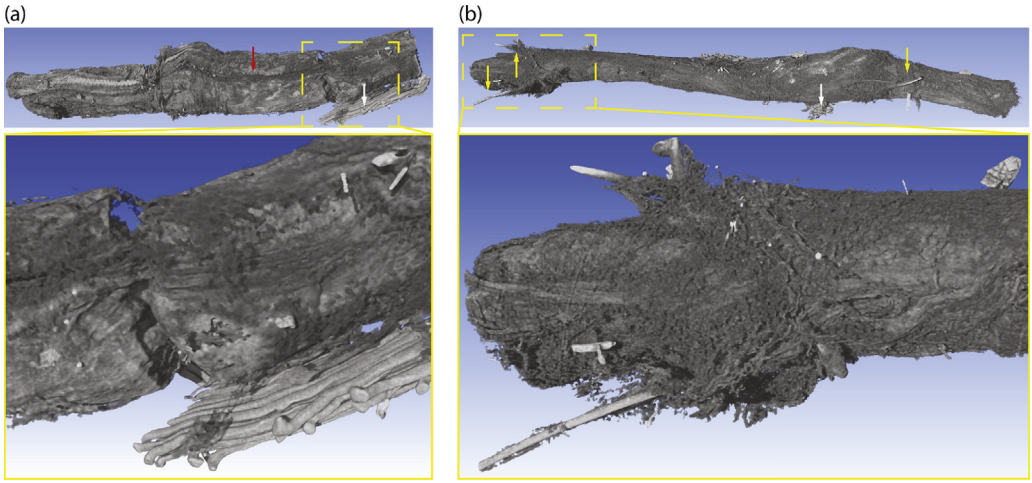

Fig. 1. Three dimensional visualization of tomography data from a healthy (a) and a reconstructed nerve (b), with a length of approximately 8 and 15 mm, respectively. The surrounding paraffin has been made digitally transparent prior to this 3D rendering. The red-colored arrow indicates the surface groove between the major nerve fascicles and the white-colored arrows show muscle fibers on the surface of the nerves. The yellow-colored arrows indicate the two ends of the reconstructed nerve.

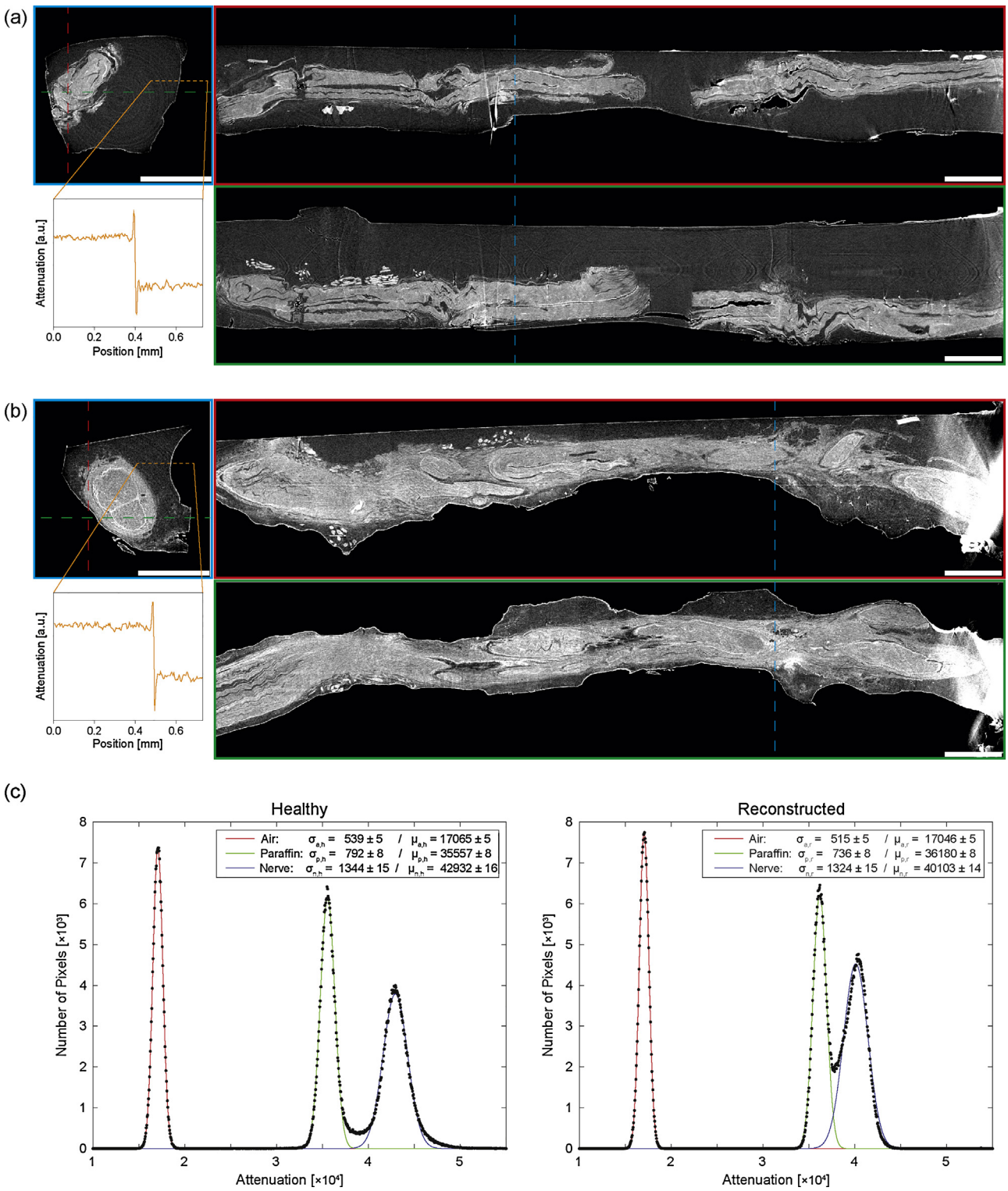

Fig. 2. Cross sectional and longitudinal views of healthy (a) and regenerated (b) rat sciatic nerves respectively, together with selected line plots and histograms of selected regions of interest (c). The green, red and blue dashed lines and subfigure frames show the relative position of the depicted cuts through the 3D datasets. The included line plots are taken along the orange-colored dashed lines. In the longitudinal views, the proximal and distal ends of the nerves are located at 2 mm from the right and left borders of the images, respectively. In these views, one recognizes that the healthy nerve is comprised of two parts, which show only a small gap and are embedded into paraffin together. The black dots in the histogram indicate the number of pixels corresponding to a specific attenuation value and the curves are Gaussians fitted to the experimental data, corresponding to air (red), paraffin (green) and nerve (blue). The attenuation values are related to the current setup and do not represent the physical quantity used for monochromatic radiation. The scale bars correspond to a length of 1 mm.

by the existence of two main nerve fascicles. More muscle fibers are seen attached to the nerve surface (white-colored arrow), compared to the regenerated nerve. The mean diameter of these muscle fibers is around 50 μm, in reasonable agreement with the literature values (Alnaqeeb and Goldspink, 1987). A zoom-in onto the surface of the healthy nerve (Fig. 1a, bottom) better reveals their rod-like structure and parallel arrangement.

3.2. Structural analysis of reconstructed nerve

Another distinctive advantage of 3D tomographic data is the ability to select any virtual cutting plane, as illustrated in Fig. 2, where three orthogonal cutting planes at once are used to better reveal the internal structures and the degree of organization of the nerves investigated. The white color structures appearing in longitudinal and cross-sectional images of both nerve samples indicate the axons and associated myelin tissue (Hopkins et al., 2015; Pixley et al., 2016). Fission-like-structures existing in the cross sections show the organization of the nerve fascicles in all the tissue samples. The epineurium and perineurium membranes as well as the vessels are depicted white, due to a higher local X-ray absorption, while the surrounding medium (air) is shown as black, due to minimal X-ray absorption. Paraffin surrounding the nerves is shown in gray, according to the local X-ray absorption.

For the reconstructed nerve data, the cross-sectional view obtained from its proximal end, reveals the existence of two main nerve fascicles, divided by one prominent perineurium membrane. No major vessel can be detected in this cross-sectional view, as easy as in the healthy nerve (Fig. 2). In addition, the connective tissue surrounding the fascicles is enveloping them more closely than for the case of the healthy nerve, where both the connective tissue and the epineurium membrane are separated from the four main nerve fascicles visible and at places show differing X-ray absorption.

The longitudinal views clearly revealed the internal structures such as the fascicle orientation and 3D organization. In the reconstructed nerves, the fascicles are not as easily distinguishable, as it is the case for their healthy counterpart. Moreover, the reconstructed nerve shows a random arrangement of fascicles, that, especially around its proximal and distal end becomes so complicated that some of them are perpendicular to the major nerve axis. Both nerve thickness and degree of fascicle anisotropy are maximized at the proximal and distal nerve ends, compared to its thinner middle section.

Fig. 2 also shows two line plots through the selected cross sectional cuts of the 3D dataset, indicating a spatial resolution close to the effective pixel size for both measurements. Histograms of the local X-ray absorption from selected regions of the two datasets are also presented. They contain three Gaussian peaks corresponding to air (red), paraffin (green) and nerve tissue (blue), which can be identified by intensity thresholding (Müller et al., 2002). The area under the histogram curve includes all voxels of the selected region of interest (ROI), and the area under each peak provides the volume of its related specimen component. For our measurements, the fact that the Gaussians fit the data very well indicates the meaningful applicability of photon statistics. For each Gaussian, the expectation value μ gives the peak position corresponding to a specific component and the standard deviation σ characterizes how broad the distribution is. Based on these parameters, the signal-to-noise ratio (SNR) of each specific component was calculated as: $\mathrm{SNR\ (component)} = |\mu_{\mathrm{component}} - \mu_{\mathrm{air}}|/\sigma_{\mathrm{air}}$. The SNR for both paraffin and nerve was almost equal for both measurements ($\mathrm{SNR_{healthy}(paraffin)} = 34.31 \pm 0.02$; $\mathrm{SNR_{regenerated}\ (paraffin)} = 37.12 \pm 0.02$, $\mathrm{SNR_{healthy}(nerve)} = 47.99 \pm 0.03$; $\mathrm{SNR_{regenerated}\ (nerve)} = 44.74 \pm 0.03$).

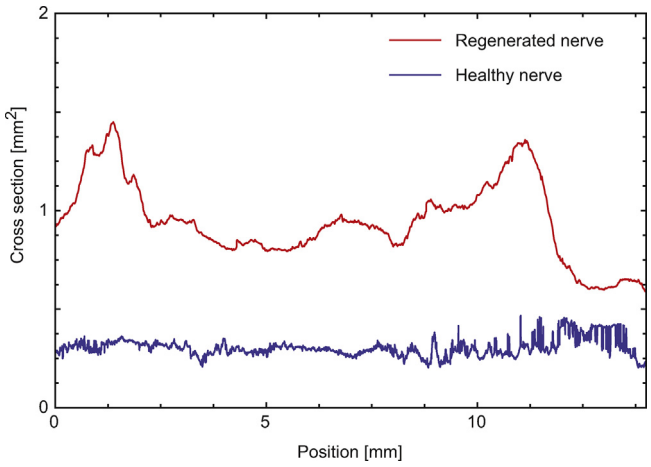

Fig. 3. Cross sectional area along two representative nerves. The healthy nerve shows an almost constant value, whereas the regenerated nerve exhibits characteristic modulations.

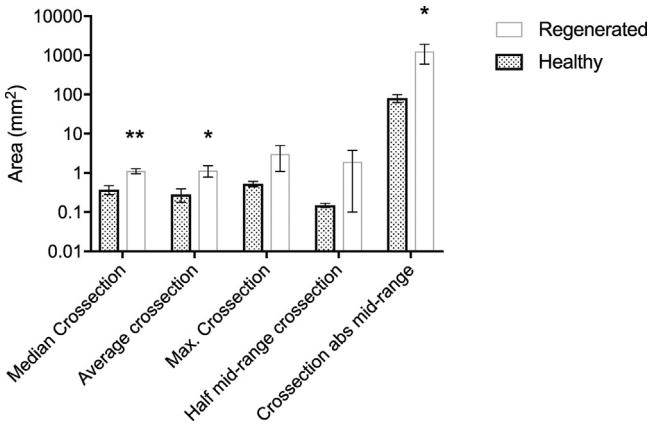

Fig. 4. Comparison of geometrical parameters for three healthy and three regenerated nerves, calculated automatically after nerve segmentation. Single asterisk indicates a p-value smaller than 0.05 and double asterisk indicates a p-value smaller than 0.01.

3.3. Nerve thickness profile

After the nerve has been segmented from its surrounding paraffin, plotting the cross-sectional area over the nerve length provides useful information on the nerve regeneration process, as seen in Fig. 3, where one representative healthy and one reconstructed nerve are presented from each group. There are two distinctive peaks in the curve of the reconstructed nerve, indicating the proximal (left) and distal (right) end. The region between these two peaks corresponds to the reconstructed nerve segment. For the case of a healthy nerve, its thickness profile revealed by measurement of cross-sectional area remains relatively constant along its entire length.

3.4. Nerve geometry

We have also calculated several geometrical parameters for the nerves investigated, in an automated process. Fig. 4 shows the results of the two groups of healthy and reconstructed nerves ($n = 3$), as well as their comparison. The parameters chosen for the investigation were the median and maximum cross section, the average cross sections (defined as volume/length), the half mid-range cross-section (defined as the distance of maximum to the median) and the cross section abs mid-range (defined as the sum of the distance of each cross section along the nerve length to

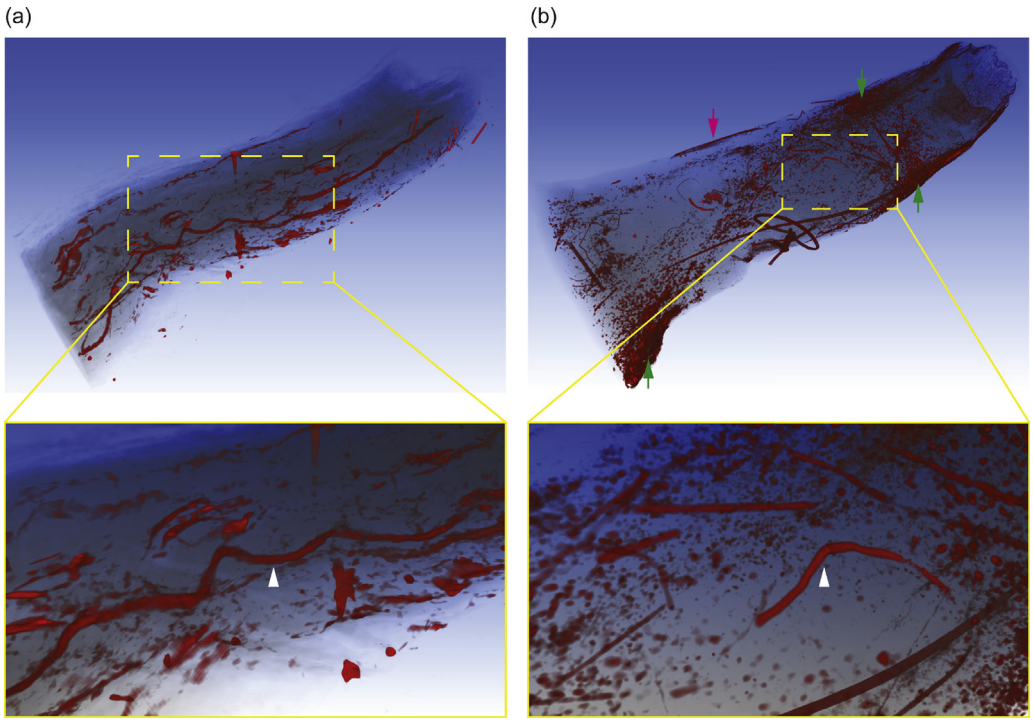

Fig. 5. Intensity-thresholded vessels of a healthy (a) and a reconstructed (b) nerve, with a length of approximately 3 and 7 mm, respectively. The surrounding paraffin has been made digitally transparent and the nerve volume has been made semi-transparent to allow for a better visualization of the vessel structure. The diameter of the vessels indicated by the white-colored arrows is approximately 0.04 and 0.02 mm for the healthy and the reconstructed nerve, respectively.

the median). In detail, a strongly statistically significant difference was observed between the reconstructed and the healthy group for the median cross section ($p = 0.0026$). There was also a statistically significant difference between the two groups for the average cross section (defined as volume/length) and the cross section abs (absolute) mid-range (defined as the sum of the distance of the cross section at each position along the nerve to the median cross section), with $p = 0.0178$ and $p = 0.0419$, respectively. Finally, a tendency for a statistically significant difference between the two groups was found for the maximum cross section ($p = 0.0890$).

3.5. Vascular regrowth

Vessels show a higher intensity value than paraffin or nervous tissue, namely around 44,000 for the histograms presented in Fig. 2. Due to a low number of vessel voxels the histogram does not reveal them separately. The vessel network is visualized in Fig. 5 using thresholding. Intensity thresholding revealed interesting observations associated with vascular regrowth. The results of this segmentation process are seen in Fig. 5, revealing the vascular network of a healthy (Fig. 5a) and reconstructed (Fig. 5b) nerve, respectively. In detail, for the case of the reconstructed nerves, the mean diameter of the detected vessels is smaller, compared to healthy nerves. In addition, a quick overview of the reconstructed nerve (Fig. 5b) revealed the existence of several small signals characterized by high X-ray absorption at the proximal and distal nerve ends (green-colored arrows). These structures may indicate haematomas.

Inside the reconstructed nerve, the morphology and organization of vessels appeared to be heterogeneous. The visual inspection of the high-resolution CT data indicates that the nerve ends contain a less organized vessel structure and have random orientation. It is difficult to prove this observation, since the number of segmented vessels is relatively low. Vessel density is also higher near the two ends of the nerve. In contrast, the region between the proximal and distal parts of the reconstructed nerve exhibits a more organized vessel structure; vessels are generally bigger in diameter compared to the ones at the nerve ends and are less frequently branched. They are mostly parallel one to another, following the nerve axis and residing very close to its surface (magenta-colored arrow).

4. Discussion

4.1. Spatial resolution and image contrast

The lineplots presented in Fig. 2 run along the paraffin/air edge and were used to determine the spatial resolution close to the pixel size, as described earlier (Thurner et al., 2004). From the mean and standard deviation values of the Gaussians fitted to the histograms presented in Fig. 2, the SNR for the microstructures was calculated (Schulz et al., 2012). The SNR was almost identical for the case of paraffin (considered to be a homogeneous structure) in both measurements. Together with the fact that spatial resolution was also found similar for both measurements, scanning quality is considered consistent. Compared to US and MRI, which are the modalities of choice for peripheral nerve 3D imaging in clinical practice (Willsey et al., 2017), the spatial resolution achieved in this study is at least two orders of magnitude better in each of the three orthogonal directions. Compared to recent similar μCT studies, e.g. Hopkins et al. (2015), Pixley et al. (2016), spatial resolution is at least an order of magnitude better in each orthogonal direction. Although our approach needs no staining agent at all, the obtained tomogram contrast is also greatly increased, allowing for the discrimination between nerve fascicles and connective tissue, an unsolved problem for similar studies up until now (Hopkins et al., 2015). The superior image quality makes even an automated nerve segmentation and extraction of quantitative parameters possible.

In this study, the most notable difference between the two measurements is the better separation of the paraffin and nerve peak of the histograms for the case of the healthy nerve compared to the regenerated one, as seen in the images of Fig. 2. We have already some indications that during the first days of the

sample being embedded in paraffin, contrast difference between structures increases as the time passes, most probably due to an ongoing perfusion progress. It is also possible, that a combination of an existing difference between groups and a preparation effect could have taken place; one hypothesis is, that the regenerating nerve, due to less compact bundle packing or myelin maturity, is physically less stable and therefore gets more affected during the dehydration and subsequent paraffin perfusion.

4.2. Thickness profile along the nerves

Diagrams as shown in Fig. 3 can be used to assess the length of the zones in the regenerating nerves, as well as quickly reveal possible segmentation errors. For example, the numerous small spikes of the cross-sectional area along the end of the healthy nerve were caused by suboptimal segmentation, due to cone beam artifacts.

While the fast fluctuations in the amplitude are caused by improper segmentation, the high and slow modulation of the regenerating nerve cross section compared to its healthy counterpart can be explained by the mechanism of nerve damage and regeneration itself. An increased cross-sectional area is seen, as expected, in the proximal and distal ends of the reconstructed nerve, which may indicate occurrence of hemorrhage, inflammation and scarring (Fig. 3). Also as expected, the regenerated area is found to be relatively thinner, as seen for the case of the sample displayed in Fig. 1b. The two bundles observed in the cross-sectional view are not well separated and are ultimately joined further along the nerve, so that at the thinnest part of the regenerated region, all fascicles are enclosed by one single perineurium membrane.

4.3. Geometry of reconstructed nerve tissue

It should be noted that the calculated nerve cross-sectional area was taken with respect to the plane perpendicular to the rotation axis of the sample and not to the nerve centerline. For our case this only has a minor effect on the results, because the nerves were straightened as much as possible prior to embedding and then mounted with the major nerve axis parallel to the rotation axis. Even though the median cross section has the strongest difference between the two groups in terms of statistical significance, the average cross section (volume/length) can sometimes be a more preferable parameter for comparison, since it is more robust with respect to how the sample is embedded or mounted.

Cross section abs mid-range is a more robust parameter compared to the half mid-range cross section because it ignores the intra-group differences in nerve size and is directly affected by the existence of transition zones in the regenerated nerves. This is because the former takes the difference of the cross section at every point along the nerve compared to its median cross section, while the later is merely the difference of only two values, namely maximum and median cross section of the nerve.

To be able to compare geometrical parameters, all muscle or connective tissue around the nerve has to be cleared as much as possible during extraction. The regenerated nerves must also be cut with similar endpoints, e.g. using the stitches as guides.

4.4. Interpretation and challenges of vessel analysis

The visual inspection of the CT data indicates that vessels smaller than the voxel size can be detected due to the partial volume effect. Their high intensity is mainly a result of the remaining dehydrated blood in the vessel lumen. An elaborate, automated segmentation of the entire vessel tree remains an open challenge. Given that no contrast agent was used, the non-connected vessel network visualized can be caused by inhomogeneous vessel perfusion by paraffin, probably due to trapped air inside the vessels. Nevertheless, there is a clear tendency for more, shorter vessel fragments in the reconstructed nerve ends that can be explained by the angiogenesis at this sites as a response to trauma and as a basis for subsequent regeneration. In addition to that, it is very probable that the highly X-ray absorbing features filling large areas at the reconstructed nerve ends are caused by haemosidirin deposits due to hemorrhage at these areas.

5. Conclusions

We have achieved a 3D visualization of regenerated nerves with true micrometer resolution using a procedure that allows subsequent cutting and staining. Fine details of morphology and microanatomy of nerve tissue were visualized, owing to improved imaging procedure and an updated data processing. The method has been validated with a sufficient number of samples to provide findings with statistical significance. The quantitative parameters of regenerated nerves detailed in this study provide a suitable measure for assessing the quality of nerve regeneration with a focus on high-throughput analysis.

Conflicts of interest

The authors declare no conflict of interest.

Acknowledgments

The authors thank Stephan Frank and Jürgen Hench of the Neuropathology Department, Basel University Hospital for allowing the use of histological equipment, as well as Sascha Martin and Stefan Gentsch of the Mechanics Shop, Physics Department, University of Basel, for fabricating the customized sample holders. The project was supported by SNSF projects144535 and 133802.

References

Alnaqeeb, M.A., Goldspink, G., 1987. Changes in fibre type, number and diameter in developing and ageing skeletal muscle. J. Anat. 153, 31–45 http://www.ncbi.nlm.nih.gov/pmc/articles/PMC1261780/.

Bikis, C., Degrugillier, L., Deyhle, H., Schulz, G., Schweighauser, G., Hench, J., Müller, B., Madduri, S., Hieber, S.E., 2016. Using laboratory μCT for assessing peripheral nerve regeneration. Eur. Cells Mater. 32, 30.

Bikis, C., Thalmann, P., Degrugillier, L., Schulz, G., Müller, B., Kalbermatten, D.F., Madduri, S., Hieber, S.E., 2017. Three-dimensional and non-destructive characterization of nerves inside conduits using laboratory-based micro computed tomography. J. Neurosci. Methods 294, 59–66.

Garg, K., Aggarwal, A., Srivastava, D.N., Jana, M., Sharma, R., Gamanagatti, S., Kumar, A., Kumar, V., Malhotra, R., Goyal, V., Garg, K., 2017. Comparison of Different Sequences of MRI and Ultrasongram with Nerve Conduction Studies in Peripheral Neuropathies. World Neurosurgery.

Haftek, J., 1976. Autogenous cable nerve grafting instead of end to end anastomosis in secondary nerve suture. Acta Neurochir. (Wien) 34, 217–221.

Hopkins, T.M., Heilman, A.M., Liggett, J.A., LaSance, K., Little, K.J., Hom, D.B., Minteer, D.M., Marra, K.G., Pixley, S.K., 2015. Combining micro-computed tomography with histology to analyze biomedical implants for peripheral nerve repair. J. Neurosci. Methods 255, 122–130.

Hsu, S.H., Kuo, W.C., Chen, Y.T., Yen, C.T., Chen, Y.F., Chen, K.S., Huang, W.C., Cheng, H., 2013. New nerve regeneration strategy combining laminin-coated chitosan conduits and stem cell therapy. Acta Biomater. 9, 6606–6615.

Johnson, E.O., Zoubos, A.B., Soucacos, P.N., 2005. Regeneration and repair of peripheral nerves. Injury 36 (Suppl. 4), S24–9.

Kannan, R.Y., Salacinski, H.J., Butler, P.E.M., Seifalian, A.M., 2005. Artificial nerve conduits in peripheral-nerve repair. Biotechnol. Appl. Biochem. 41, 193–200.

Kingham, P.J., Terenghi, G., 2006. Bioengineered nerve regeneration and muscle reinnervation. J. Anat. 209, 511–526 http://www.ncbi.nlm.nih.gov/pmc/articles/PMC2100355/.

Madduri, S., Feldman, K., Tervoort, T., Papaloïzos, M., Gander, B., 2010a. Collagen nerve conduits releasing the neurotrophic factors GDNF and NGF. J. Control. Release 143, 168–174 http://www.sciencedirect.com/science/article/pii/S0168365909008621.

Madduri, S., di Summa, P., Papaloïzos, M., Kalbermatten, D., Gander, B., 2010b. Effect of controlled co-delivery of synergistic neurotrophic factors on early nerve regeneration in rats. Biomaterials 31, 8402–8409 http://www.sciencedirect.com/science/article/pii/S0142961210008951.

Madduri, S., Gander, B., 2012. Growth factor delivery systems and repair strategies for damaged peripheral nerves. J. Control. Release 161, 274–282.
Moore, A.M., Kasukurthi, R., Magill, C.K., Farhadi, H.F., Borschel, G.H., Mackinnon, S.E., 2009. Limitations of conduits in peripheral nerve repairs. Hand (New York, N.Y.) 4, 180–186.
Müller, B., Thurner, P., Beckmann, F., Weitkamp, T., Rau, C., Bernhardt, R., Karamuk, E., Eckert, L., Brandt, J., Buchloh, S., Wintermantel, E., Scharnweber, D., Worch, H., 2002. Nondestructive three-dimensional evaluation of biocompatible materials by microtomography using synchrotron radiation. Proc. SPIE 4503, 178–188, http://dx.doi.org/10.1117/12.452843.
Pixley, S.K., Hopkins, T.M., Little, K.J., Hom, D.B., 2016. Evaluation of peripheral nerve regeneration through biomaterial conduits via micro-CT imaging. Laryngoscope Investig. Otolaryngol. 1, 185–190.
Schulz, G., Weitkamp, T., Zanette, I., Pfeiffer, F., Müller-Gerbl, M., David, C., Müller, B., 2012. Asymmetric rotational axis reconstruction of grating-based X-ray phase contrast tomography of the human cerebellum. Proc. SPIE 8506, 850604, http://dx.doi.org/10.1117/12.928487.
Stalder, A.K., Ilgenstein, B., Chicherova, N., Deyhle, H., Beckmann, F., Müller, B., Hieber, S.E., 2014. Combined use of micro computed tomography and histology to evaluate the regenerative capacity of bone grafting materials. Int. J. Mater. Res. 105, 679–691, http://dx.doi.org/10.3139/146.111050.
Stang, F., Fansa, H., Wolf, G., Reppin, M., Keilhoff, G., 2005. Structural parameters of collagen nerve grafts influence peripheral nerve regeneration. Biomaterials 26, 3083–3091.
Thurner, P., Beckmann, F., Müller, B., 2004. An optimization procedure for spatial and density resolution in hard X-ray micro-computed tomography. Nucl. Instrum. Methods Phys. Res. B 225, 599–603 http://www.sciencedirect.com/science/article/pii/S0168583X04007980.
Walker, F.O., 2017. Ultrasonography in peripheral nervous system diagnosis. Contin. (Minneap. Minn.) 23, 1276–1294.
Weis, J., Brandner, S., Lammens, M., Sommer, C., Vallat, J.M., 2012. Processing of nerve biopsies: a practical guide for neuropathologists. Clin. Neuropathol. 31, 7–23.
Willsey, M., Wilson, T.J., Henning, P.T., Yang, L.J.S., 2017. Intraoperative ultrasound for peripheral nerve applications. Neurosurg. Clin. N. Am. 28, 623–632.
Wu, C., Wang, G., Zhao, Y., Hao, W., Zhao, L., Zhang, X., Cao, J., Wang, S., Chen, W., Chan, Q., Zhao, B., Chhabra, A., 2017. Assessment of tibial and common peroneal nerves in diabetic peripheral neuropathy by diffusion tensor imaging: a case control study. Eur. Radiol. 27, 3523–3531.
Yang, Y., Ding, F., Wu, J., Hu, W., Liu, W., Liu, J., Gu, X., 2007. Development and evaluation of silk fibroin-based nerve grafts used for peripheral nerve regeneration. Biomaterials 28, 5526–5535.